

Water Resources Research

RESEARCH ARTICLE

10.1029/2019WR025034

Key Points:

- The factors controlling ground rupture generation accompanying groundwater pumping have been investigated by an advanced numerical model
- The rupture evolution is classified in two occurrences: a first where the rupture remains limited at depth and land surface and a second where the rupture propagates vertically
- A multivariate analysis of the model outcomes provides a general methodology for a preliminary evaluation of possible rupture development

Correspondence to:

P. Teatini,
pietro.teatini@unipd.it

Citation:

Frigo, M., Ferronato, M., Yu, J., Ye, S., Galloway, D., Carreón-Freyre, D., & Teatini, P. (2019). A parametric numerical analysis of factors controlling ground ruptures caused by groundwater pumping. *Water Resources Research*, 55. <https://doi.org/10.1029/2019WR025034>

Received 21 FEB 2019

Accepted 20 OCT 2019

A Parametric Numerical Analysis of Factors Controlling Ground Ruptures Caused by Groundwater Pumping

Matteo Frigo¹, Massimiliano Ferronato¹, Jun Yu², Shujun Ye³ , Devin Galloway⁴ , Dora Carreón-Freyre⁵, and Pietro Teatini¹ 

¹Department of Civil, Architectural, and Environmental Engineering, University of Padova, Padova, Italy, ²Key Laboratory of Earth Fissures Geological Disaster, Ministry of Land and Resources, Geological Survey of Jiangsu Province, Nanjing, China, ³School of Earth Sciences and Engineering, Nanjing University, Nanjing, China, ⁴Earth Science Processes Division, Water Mission Area, United States Geological Survey, Indianapolis, IN, USA, ⁵Centro de Geociencias, Universidad Nacional Autónoma de México, Queretaro, Mexico

Abstract A modeling analysis is used to investigate the relative susceptibility of various hydrogeologic configurations to aseismic rupture generation due to deformation of aquifer systems accompanying groundwater pumping. An advanced numerical model (GEPS3D) is used to simulate rupture generation and propagation for three typical processes: (i) reactivation of a preexisting fault, (ii) differential compaction due to variations in thickness of aquifer/aquitard layers constituting the aquifer system, and (iii) tensile fracturing above a bedrock ridge that forms the base of the aquifer system. A sensitivity analysis is developed to address the relative importance of various factors, including aquifer depletion, aquifer thickness, the possible uneven distribution and depth below land surface of the aquifer/aquitard layers susceptible to aquifer-system compaction, and the height of bedrock ridges beneath the aquifer system which contributes to thinning of the aquifer system. The rupture evolution is classified in two occurrences. In one, the rupture develops at either the top of the aquifer or at land surface and does not propagate. In the other, the developed rupture propagates from the aquifer top toward the land surface and/or from the land surface downward. The aquifer depth is the most important factor controlling rupture evolution. Specifically, the probability of a significant rupture propagation is higher when the aquifer top is near land surface. The numerical results are processed by a statistical regression analysis to provide a general methodology for a preliminary evaluation of possible ruptures development in exploited aquifer systems susceptible to compaction and accompanying land subsidence. A comparison with a few representative case studies in Arizona, USA, China, and Mexico supports the study outcomes.

1. Introduction

Ground rupture, with fracture opening (Earth fissure; Figure 1a) or small to large vertical offset (faulting; Figure 1b), is a geomechanical process that may be associated with groundwater pumping from unconsolidated sedimentary aquifer systems. Apart from a few occurrences, for example those in Suzhou-Wuxi-Changzhou area, Yangtze River delta, China (Ye et al., 2018; Zhang et al., 2016), ground ruptures associated with groundwater pumping generally develop in arid or semiarid basins. The largest densities of ground ruptures are located in Arizona, USA (Conway, 2016; Jachens & Holzer, 1979), central Mexico (Carreón-Freyre, 2010; Carreón-Freyre et al., 2016; Teatini et al., 2018), northern China (Li et al., 2000; Peng et al., 2016), and Iran (Ziaie et al., 2009), where the average annual precipitation is 200, 500, 550, and 300 mm, respectively.

Interestingly, the occurrence of ground ruptures caused by groundwater pumping is always associated with exploited aquifer systems strongly affected by aquifer-system compaction and accompanying land subsidence, but not all exploited aquifer systems affected by land subsidence experience ground ruptures. Shanghai in China (Ye et al., 2016), Ravenna in Italy (Teatini et al., 2005), and Jakarta in Indonesia (Abidin et al., 2011) are only a few sites well known for land subsidence in excess of 1 m where ground ruptures have not been reported. Only a few ground ruptures have been recorded in the San Joaquin Valley in California, despite the occurrence of more than 8.5 m of land subsidence (Galloway & Riley, 1999). The generation and propagation of ruptures requires the development of failure conditions, that is, tensile and/or shear stress not supported by shallow alluvial sediments. Stress fields of these kinds have been documented by a number of modeling analyses aimed at understanding the rupture occurrence at specific sites in Mexico



Figure 1. Examples of earth ruptures: (a) a fissure disrupting a road in Cochise County, Arizona, USA (photo by Mike Mahan, Arizona Geological Survey, August 2011); (b) the San Francisco monastery in Celaya, Mexico, cut in two blocks to preserve the structure by accommodating the sliding of a preexisting fault reactivated by groundwater pumping; and (c) structural damage to streets and buildings in Xian, China, as of 2014 due to ground faulting (modified after Gambolati & Teatini, 2015). The rupture is mainly characterized by opening (~ 0.5 m) in (a), sliding (~ 1.2 m) in (b), and both sliding (~ 0.2 m) and opening (~ 0.3 m) in (c).

(Carreón-Freyre et al., 2016; Ochoa-González et al., 2018; Pacheco et al., 2006), China (Ye et al., 2018), and Nevada (Hernandez-Marin & Burbey, 2010, 2012) and Arizona (Panda et al., 2015) in the USA. Recently, Choubin et al. (2019) applied a machine learning approach to investigate the ground rupture hazard in the semiarid Yazd-Ardakan plain, central Iran. They found that the main factor driving rupture occurrence is elevation: in their study area low elevations with low precipitation, high groundwater withdrawal, high well density, high road density, and the presence of Quaternary sediments are associated with a high hazard of ground ruptures.

Important economic, social, and environmental damages are associated with ground ruptures: failure of borehole casings, pipelines used for oil and gas conveyance, canals used for water conveyance, and structural damages to surface structures (e.g., roadways, runways, dams and levees, houses, and buildings, including historical heritage structures such as palaces and churches; e.g., Rucker et al., 2019). Generally, ruptures caused by groundwater pumping develop aseismically due to the poorly consolidated nature of deposits constituting the susceptible aquifer systems. Seismic events have been associated with aquifer overexploitation in a few studies (e.g., González et al., 2012; Kundu et al., 2015), but induced seismicity is beyond the scope of this study. Also ground ruptures associated with mining (e.g., Klose, 2007) and fault reactivation due to hydrocarbon production (e.g., van Wees et al., 2014) are processes related to those of interest here but are not addressed in this work.

This contribution is aimed at investigating the hydrogeologic settings and aquifer depletion conditions that are most prone to the inception and propagation of ground ruptures. Using a numerical model we analyze the three main hydrogeologic settings favoring rupture generation, qualitatively delineated by Sheng and Helm (1998) and Sheng et al. (2003): (i) an aquifer system bounded by outcropping rocks; (ii) differential compaction due to an abrupt variation in thickness of the exploited aquifer system, for example in correspondence with a pre-existing fault; and (iii) tensile fracturing above a bedrock ridge (Figure 2). A parametric analysis is carried out for each setting to identify the geometric configurations that likely cause rupturing, and to quantify rupture depth in relation to fluid-pressure depletion in the pumped aquifer.

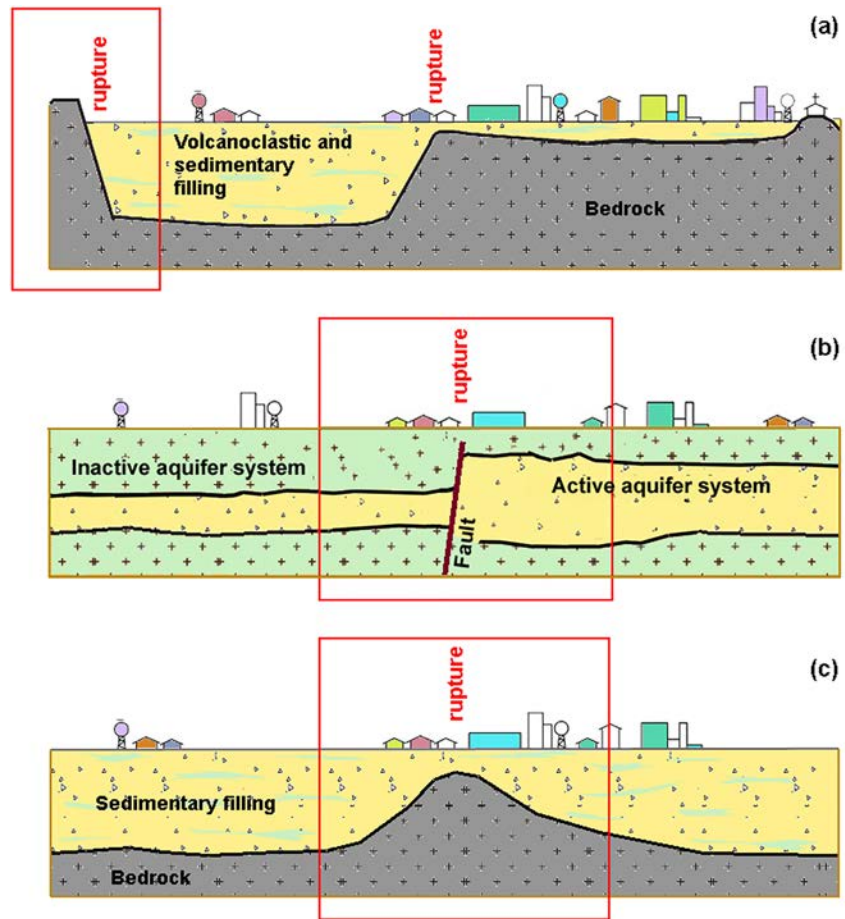


Figure 2. Conceptual schematizations of geological settings which represent real-world settings where ground ruptures are known to occur: (a) sedimentary and volcanoclastic materials filling faulted basins, (b) aquifer systems with abrupt thickness changes, and (c) buried bedrock ridge that forms the base of a sedimentary aquifer system.

The analysis of the failure processes with a physically based approach requires advanced numerical approaches developed in the field of discontinuum mechanics. The stable and accurate simulation of the activation and motion of a discontinuity is still an active area of research. In this work, we use the Lagrange-multiplier based numerical formulation developed by Franceschini et al. (2016) and implemented in the GEPS3D geomechanical simulator (Isotton et al., 2019; Janna et al., 2012). A rupture is simulated as a pair of inner surfaces included in a three-dimensional (3-D) geological formation and Lagrange multipliers are used to prescribe the contact constraints. The process is controlled by the classical Mohr–Coulomb failure criterion, and the frictional work dissipated by the relative motion of the pair of inner surfaces is governed by the Principle of Maximum Plastic Dissipation (Simo & Hughes, 2000; Wriggers, 2005). A similar approach based on contact interfaces is implemented in advanced, commercial multipurpose/multiphysics simulators, for example, Plaxis (Plaxis, 2017) and Abaqus (<https://www.3ds.com/products-services/simulia/products/abaqus/>, accessed 22 September 2019). Because of numerical efficiency (Franceschini et al., 2019) and accuracy of the approach implemented, as recently tested by Ye et al. (2018) in the simulation of a ground rupture at Wuxi, China, we have elected to use GEPS3D.

Following a brief description of the modeling approach, the model development and results for the three simulated test cases are presented in detail. The results of the numerical simulations along with a multivariate analysis of the results are discussed to derive a more general understanding of the principal factors governing ground rupture. Then, a few sites worldwide that are characterized by ground rupturing and where hydrogeologic information is available are discussed to contextualize the results of the present study.

2. Modeling Approach

2.1. Mathematical and Numerical Model

A rupture developing in a geological formation can be mathematically idealized as a discontinuity within a 3-D porous body identified by a pair of friction surfaces in contact with each other. The contact is subject to a set of conditions, such as friction and impenetrability of solid bodies, so that the overall problem can be mathematically described as a constrained minimization problem for the total potential energy of the system. A continuum approach, typically used for modeling aquifer-system compaction and land subsidence (e.g., Hoffman et al., 2003; Leake & Galloway, 2007; Ye, Luo, et al., 2016), cannot be used to simulate contact problems.

The friction law commonly used to describe the rupture behavior at the macroscale is based on the classical Mohr–Coulomb framework (Jaeger & Cook, 1979). For a given 3-D porous domain $\Omega \subset \mathbb{R}^3$ with the external frontier $\Gamma \subset \mathbb{R}^2$, a rupture is described by a well-defined internal boundary Γ_f consisting of two overlapping surfaces Γ_f^- and Γ_f^+ with unit normal vector \mathbf{n}_f , conventionally oriented from Γ_f^- to Γ_f^+ . The classical Coulomb frictional condition on the contact surfaces prescribes that, for every instant of time, the following inequality holds true for the surface $\Phi(\mathbf{t})$:

$$\Phi(\mathbf{t}) = \|\mathbf{t}_T\|_2 - (c - t_N \tan \varphi) \leq 0 \quad (1)$$

where t_N and \mathbf{t}_T are the normal and tangential components of the traction vector \mathbf{t} acting over Γ_f , that is, $\mathbf{t} = t_N \mathbf{n}_f + \mathbf{t}_T$, and c and φ are the cohesion and friction angle, respectively, used to define the limiting value $\tau_{max} = c - t_N \tan \varphi$ for the modulus of \mathbf{t}_T . Whenever the rupture is compressed, that is, $t_N < 0$, and the inequality (1) becomes an equality, a slip displacement \mathbf{g}_T between Γ_f^- and Γ_f^+ is allowed, and the tangential traction \mathbf{t}_T has a magnitude τ_{max} and direction collinear with \mathbf{g}_T , according to the Principle of Maximum Plastic Dissipation.

The impenetrability of solid bodies is prescribed by the normal contact condition:

$$t_N g_N = 0 \quad (2)$$

under the constraints $t_N \leq 0$ and $g_N \geq 0$, where g_N is the relative displacement between Γ_f^- and Γ_f^+ along the direction \mathbf{n}_f . The jump $[[\mathbf{u}]]$ of the displacement vector across Γ_f has g_N and \mathbf{g}_T as normal and tangential components, respectively:

$$[[\mathbf{u}]] = g_N \mathbf{n}_f + \mathbf{g}_T \quad (3)$$

like the traction \mathbf{t} over Γ_f . In other words, condition (2) with the definition (3) states that a normal positive displacement is allowed only if the normal traction t_N is zero; otherwise, g_N is zero.

The application of the friction law (1) and the principle of impenetrability of solid bodies (2) subdivide the inner boundary Γ_f into three portions:

1. Γ_f^{stick} , where $\Phi < 0$ and $t_N < 0$: the discontinuity is fully closed and behaves as a part of the continuum;
2. Γ_f^{slip} , where $\Phi = 0$ and $t_N < 0$: a slip displacement is freely allowed at a fixed tangential traction τ_{max} ;
3. Γ_f^{open} , where $t_N = 0$: both opening and slip displacements are freely allowed with zero traction.

The subsets above are such that $\Gamma_f = \Gamma_f^{stick} \cup \Gamma_f^{slip} \cup \Gamma_f^{open}$ with empty intersections. The determination of such subsets is part of the problem unknowns.

The minimization of the total potential energy of the porous system is carried out by a variational formulation, where the constraints (1) and (2) are prescribed by Lagrange multipliers. This way, the problem reduces to a pair of variational equalities that can be solved numerically by finite elements (Kikuchi & Oden, 1988). In this work, we use the numerical approach developed by Franceschini et al. (2016). Following the weak mixed continuum formulation of this problem, we want to find the displacement $\mathbf{u} \in \mathcal{V}$ in Ω and the traction $\mathbf{t} \in \mathcal{M}$ over Γ_f such that for every instant of the simulation:

$$\int_{\Omega} \nabla^s \mathbf{v} : \boldsymbol{\sigma}(\mathbf{u}) d\Omega - \int_{\Omega} \alpha \nabla^s \mathbf{v} : \mathbf{1} p d\Omega - \int_{\Omega} \mathbf{v} \cdot \mathbf{b} d\Omega - \int_{\Gamma} \mathbf{v} \cdot \mathbf{s} d\Gamma + \int_{\Gamma_f} \llbracket \mathbf{v} \rrbracket \cdot \mathbf{t} d\Gamma = 0 \quad (4)$$

$$\int_{\Gamma_f^{stick}} \boldsymbol{\mu} \cdot (\mathbf{n}_f \otimes \mathbf{n}_f) \cdot \llbracket \mathbf{u} \rrbracket + \boldsymbol{\mu} \cdot (\mathbf{1} - \mathbf{n}_f \otimes \mathbf{n}_f) \cdot \llbracket \dot{\mathbf{u}} \rrbracket d\Gamma + \int_{\Gamma_f^{slip}} \boldsymbol{\mu} \cdot (\mathbf{n}_f \otimes \mathbf{n}_f) \cdot \llbracket \mathbf{u} \rrbracket d\Gamma = 0 \quad (5)$$

for all vector functions $\mathbf{v} \in \mathcal{V}$ and $\boldsymbol{\mu} \in \mathcal{M}$, with \mathcal{V} and \mathcal{M} appropriate Sobolev spaces of square integrable functions with square integrable gradients (Hager et al., 2008; Kikuchi & Oden, 1988). In equations (4) and (5), $\boldsymbol{\sigma}(\mathbf{u})$ is the effective stress tensor, α the Biot coefficient, $\mathbf{1}$ the rank-2 identity tensor, p the pore fluid pressure, \mathbf{b} and \mathbf{s} are the volume and surface external forces, respectively, with ∇^s denoting the symmetric gradient operator and \otimes the dyadic product. In practice, equation (4) is the virtual work principle taking into account the contribution arising on the inner boundary Γ_f , while equation (5) prescribes in a variational form the set of constraints (1) and (2) over Γ_f . The traction \mathbf{t} over Γ_f plays the role of Lagrange multipliers. Notice that the same mathematical formalism applies for a 2-D plane strain problem as those investigated in the following. In this case the domain $\Omega \subset \mathbb{R}^2$ with the external frontier $\Gamma \subset \mathbb{R}$.

Numerical solution of equations (4) and (5) is obtained in the classical Finite Element framework. The 3-D domain is discretized into nonoverlapping tetrahedral or hexahedral elements, with discrete function spaces \mathcal{V}^h and \mathcal{M}^h replacing \mathcal{V} and \mathcal{M} . The main unknowns of the discrete problem are the displacement components at every node of the computational grid in Ω and the traction degrees of freedom along the fault/fracture surface Γ_f .

A fundamental challenge is the detection of the portions of Γ_f which belong to Γ_f^{stick} , Γ_f^{slip} , and Γ_f^{open} , which can evolve during the simulation. Indeed, only the portions where the contact is active, that is, Γ_f^{stick} and partially Γ_f^{slip} , contribute to the virtual work of the contact forces in equation (4), changing the form and size of the discrete problem. Of course, the set of active constraints is not known a priori and must be updated at every step of the simulation. In this case, an active set strategy is implemented as described algorithmically in detail by Franceschini et al. (2016). Then, a Newton loop is defined to solve the overall nonlinear problem. The resulting discrete system of equations has a generalized nonsymmetric saddle-point structure, which requires special numerical techniques to ensure convergence in large-size problems, such as those typically encountered in hydrogeologic applications of interest in this work. For more details on the solvers suitable for these applications, the reader is referred to the work by Franceschini et al. (2019).

Following the methodological approach proposed by Ye et al. (2018), the pore pressure is introduced in the discrete form of equation (4) as a source of strength obtained, for example, through a groundwater flow model. A one-way coupled approach is followed, as has been shown to be generally acceptable in hydrogeologic applications (e.g., Gambolati et al., 2000).

2.2. Model Setup

A parametric analysis is carried out in simplified aquifer systems, which represent conceptual schematizations of real-world hydrogeologic settings, for example, in Arizona, USA, Mexico, or China, where ground ruptures accompanying aquifer-system compaction and land subsidence occur. Particularly, three test cases are taken into account (Figure 2):

1. Test case A: aquifer system comprising sedimentary and volcanoclastic materials filling a graben (a depressed block of the Earth's crust bounded by opposing normal faults);
2. Test case B: aquifer system with significant heterogeneity in the distribution of compressible material and abrupt thickness changes, for example, in correspondence to a preexisting fault;
3. Test case C: aquifer system above a relatively shallow basement with the presence of a buried bedrock ridge.

The aim of this study is to investigate generation and propagation of ground ruptures caused by groundwater withdrawal from the aquifer systems in the different settings. A number of state variables, such as the ground rupture size, stress state, or deformation, are parameterized with the hydrostratigraphic variations.

For sake of simplicity, all simulations assume a linear elastic constitutive behavior for the aquifer system and the bedrock. This facilitates a clearer understanding of the main features of rupture evolution. A plane strain state condition is assumed in the three test cases. To this aim, a 50-m thick, 3-D rectangular slice 2,000-m-

wide (x direction) and 500-m-deep (z direction) domain is simulated, with displacements prevented along the direction orthogonal to x - z plane. Horizontal displacements are precluded along the lateral boundaries with a traction-free top plane and zero displacements on the bottom. A sketch of the tetrahedral discretization used in the numerical models is provided in Figure 3. A structured mesh, totaling 31,106 nodes and 150,000 elements, is generated, with the inner boundary Γ_f representing a potential ground rupture where Lagrange multipliers are introduced, highlighted in red. The size of this grid has been selected through a mesh sensitivity analysis on the variation of the numerical outcome. All test cases use the same grid, with the different problems simulated by properly changing the elemental properties. Moreover, we employ the following simplifying assumptions:

1. Groundwater flow is confined. This implies that the “active” portion of the aquifer system, that is, the units that are depleted because of groundwater withdrawal, is bounded on the top and bottom by “inactive” layers, that is, the part of the sedimentary sequence where it is assumed that the fluid pressure does not change, for example, a shallow phreatic aquifer or a deeper confined aquifer hydraulically disconnected from the pumped part of the aquifer system;
2. The fluid pressure does not change within the rupture. This is the most conservative condition, that is, the condition most favorable to the continuation of rupture opening/sliding;
3. Density gradient with depth for the solid matrix is $1,200 \text{ kg/m}^2/\text{m}$, with the minimum (maximum absolute value) σ_1 and maximum (minimum absolute value) σ_3 principal stress coinciding with the vertical σ_v and horizontal σ_h stress, respectively. Because of the shallow depth of the sedimentary sequences usually affected by ruptures associated with groundwater pumping, a normal stress regime is assumed. Therefore, the stress field is initialized based on the density gradient (σ_v) and using a minimum-to-maximum stress ratio σ_h/σ_v equal to the confinement factor $k = \frac{\nu}{1-\nu}$ (Zoback, 2007), where ν is Poisson's ratio;
4. Pore-fluid pressure variation in the active part of the aquifer system is uniform and varies linearly from 0 to -10 bar during a 10-year simulation. The active aquifer system comprises the pumped aquifers and the intervening aquitards (interbeds) where a fraction of the pressure depletion can propagate, although with a certain delay, over the 10-year simulation period. No fluid pressure change develops in the adjacent/underlying bedrock and in the inactive portion of the aquifer system;
5. Cohesion c and the friction angle φ for the rupture plane are set to 0.1 bar and 30° , respectively. The vertical uniaxial compressibility c_M and ν of the different materials, that is, rock basement, active and inactive portions of the aquifer system, are summarized for the three test cases in Table 1. These are typical values for aquifer systems exploited worldwide to supply freshwater (e.g., Conway, 2016; Ochoa-González et al., 2018; Ye et al., 2018).

For each test case, the analysis proceeds as follows. First, a continuum stress/strain analysis is performed to identify the surfaces where the rupture is more likely to develop. Then, Lagrange multipliers are introduced along those surfaces and the numerical results describing the evolution of the ground rupture are obtained for the different parameter configurations. Finally, a multivariate regression analysis is carried out to develop a statistical model able to predict the expected occurrences for a wider range of parameter values.

3. Numerical Results

3.1. Test Case A

3.1.1. Model Outcome

This test case conceptualizes the hydrogeologic configuration shown in Figure 2a. The problem domain is schematically described in Figure 4. An outcropping rock structure bounds a sedimentary and volcanoclastic depositional sequence, with an active aquifer system bounded by inactive layers on its top and bottom. This configuration conceptualizes the geological setting where ground ruptures occur in Casa Grande, Arizona, USA (Jachens & Holzer, 1982).

First, the continuum stress-strain analysis is carried out. Dimensionless displacement \mathbf{u}^* and effective stress $\boldsymbol{\sigma}^*$ components are considered:

$$u_i^* = \frac{u_i}{s}, \quad \sigma_{ij}^* = \frac{\sigma_{ij}}{\Delta p}, \quad i, j = x, y, z \quad (7)$$

where $s = c_M \cdot h \cdot \Delta p$ is the compaction of the active aquifer, with Δp the pore-fluid pressure change, h the active aquifer thickness, and c_M the uniaxial vertical compressibility. The pore pressure decrease due to

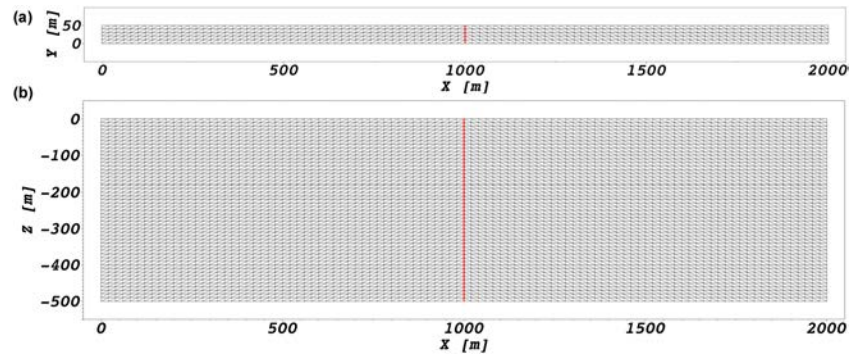


Figure 3. (a) Horizontal and (b) vertical view of 3-D grid used in the modeling study. The red line represents the trace of the ground rupture where Lagrange multipliers are introduced.

groundwater extraction causes both a vertical and a lateral deformation of the aquifer system, while the adjacent bedrock, which is much stiffer than the sedimentary sequence, remains practically unaffected. The stiffness contrast induces strain/stress peaks at the boundary between the bedrock and the compacting aquifer system. As an example, this occurrence is shown in Figure 5a for the dimensionless shear stress σ_{yz}^* with $h = 60$ m and an aquifer depth $d = 250$ m. Aquifer-system compaction occurs in the active aquifer system (rightmost portion of the domain, Figure 5b), while the adjacent bedrock (leftmost part of the domain) is largely unaffected. This differential compaction can induce a potential sliding of the sedimentary deposits with respect to the bedrock, with the boundary between the aquifer system and bedrock becoming a possible surface of rupture. Thus, the inner boundary Γ_f is inserted along this vertical plane, which is discretized by 500 triangular elements.

The effect of the hydrogeologic setting on the possibility of rupture development is tested by varying the aquifer depth d and thickness h (Figure 4) in the ranges from 50 to 300 m and from 60 to 360 m, respectively, which are common intervals of exploited aquifer systems. The outcome of the numerical simulations provides evidence that two zones of Γ_f are more likely to be activated by sliding, that is, to become part of Γ_f^{slip} . One, as expected from the continuum stress-strain analysis, is close to the aquifer top and bottom, where the peaks of tangential stress are experienced, while the other is located at the ground surface. In the latter case, because the initial vertical stress σ_{v0} and the corresponding horizontal component σ_{h0} are very small owing to the small depth and overburden load, small stress variation can likely induce a shear failure and differential displacements. Horizontal contraction of the aquifer system due to fluid pressure depletion, and the consequent decrease of the stress normal to the discontinuity plane, may also cause opening. Generally, Γ_f^{open} is smaller than Γ_f^{slip} .

The rupture along Γ_f can evolve in two different ways. Figure 6, showing the evolution of Γ_f^{slip} and Γ_f^{open} together with the dimensionless slip g_T^* and opening g_N^* :

$$g_T^* = \frac{\|\mathbf{g}_T\|_2}{s} \quad ; \quad g_N^* = \frac{g_N}{s} \quad (8)$$

describe what can typically happen with a thin and/or deep aquifer, that is, small h and/or large d . In this case, the crack is confined at the aquifer depth and the rupture does not propagate toward the ground surface (Figure 6a). Moreover, for this case Γ_f does not evolve from Γ_f^{slip} to Γ_f^{open} (Figure 6c). We denote this behavior as “condition (1).” By distinction, with thick and/or shallow aquifer systems, that is, large h and/or small d , the rupture can develop from the ground surface and propagate downward, joining the deep crack at the aquifer depth (Figure 6b). In this case, the upper part of Γ_f can evolve from Γ_f^{slip} to Γ_f^{open} , allowing for a potential opening at the ground surface (Figure 6d). This second behavior is denoted as “condition (2).”

Table 1

Uniaxial Vertical Compressibility c_M and Poisson Ratio ν for the Various Lithological Units Termed “Rock,” “Active Aquifer,” and “Inactive Aquifer” Where “Active” and “Inactive” Represent the Portion of the Aquifer System Where the Pressure Change Due to Groundwater Withdrawal Occurs or Remains Unchanged, Respectively

Material	c_M (bar ⁻¹)	ν
Rock	0.5×10^{-5}	0.25
Active aquifer system	0.5×10^{-2}	0.25
Inactive aquifer system	0.5×10^{-1}	0.25

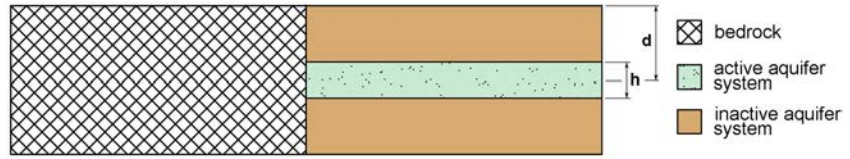


Figure 4. Test case A: Conceptual geologic setting. The aquifer system is bounded by a rocky outcrop. The active portion of the aquifer identifies the compacting layers, that is, the geologic unit where pore pressure changes because of groundwater pumping, and the inactive aquifer part of the sedimentary sequence where the pore pressure change does not propagate.

3.1.2. Multivariate Analysis

To characterize the behavior detected in test case A quantitatively as a function of h and d , a multivariate statistical analysis was performed. The state variable we considered as the model response for this test case is the “relative activation depth” $d_{r,act}$, which is defined as the vertical size of Γ_f^{slip} measured from the land surface d_{act} (Figure 6b), relative to depth of the aquifer top ($d_1 = d - h/2 > 0$):

$$d_{r,act} = \frac{d_{act}}{d_1} \quad (9)$$

Combinations of values for the pair (h,d) were considered, with $h \in [50; 300]$ and $d \in [60; 360]$ uniformly sampled by a regular step of 50 m. The combinations without a physical meaning, for example, those with $d \leq h/2$, were omitted, so that the overall data set composes 36 configurations. The outcome of 10 loading steps with a uniform pore pressure change Δp in the active aquifer system was evaluated, totaling $n = 360$ observations. For the sake of clarity, a single lumped geometrical parameter was introduced to denote each configuration. In this case, we used the ratio:

$$\eta_r = \frac{d_1}{d_2} \quad (10)$$

of the depth of the aquifer top $d_1 = d - h/2$ and bottom $d_2 = d+h/2$.

The relation between $d_{r,act}$ and the pair $(\eta_r, \Delta p)$ was investigated using a multivariate regression, which builds a 3-D surface using a least squares approach. The accuracy of the model fit was evaluated through the root-mean-square error (RMSE) and R -squared (R^2). Tables 2 and 3 provide the values of RMSE and R^2 , and the coefficients of the 3-D approximating surfaces shown in Figure 7, respectively.

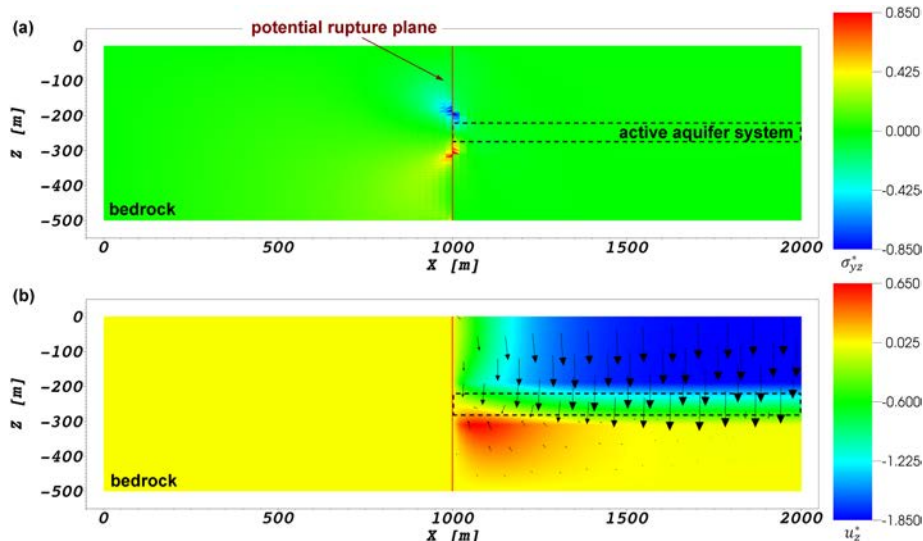


Figure 5. Test case A: (a) shear stress σ_{yz}^* and (b) vertical displacement u_z^* provided by the continuum stress-strain analysis with $h=60$ m and $d = 250$ m. A vector map showing the displacement field is provided in (b).

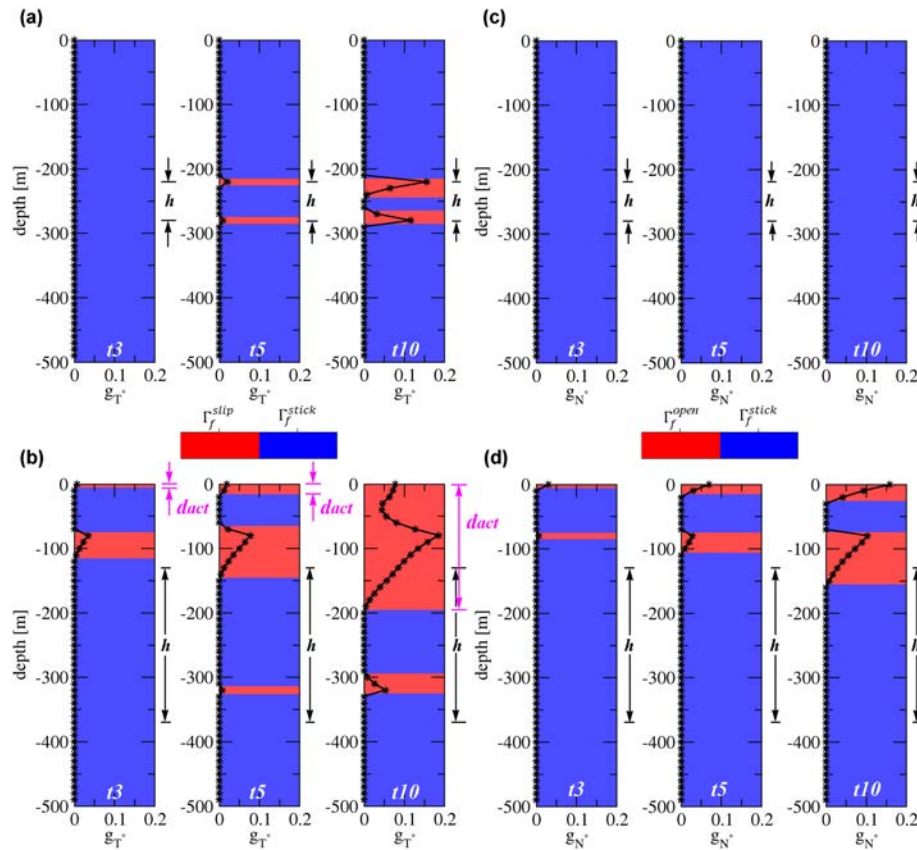


Figure 6. Test case A: (a and b) dimensionless slip g_T^* (dotted black line), sliding Γ_f^{slip} , and close Γ_f^{stick} areas (red and blue zones) for the 3rd, 5th, and 10th loading steps (denoted as $t3$, $t5$, and $t10$ in the figure) obtained for (a) $h = 60$ m, $d = 250$ m and (b) $h = 240$ m, $d = 250$ m. (c and d) Similar plots are shown for the dimensionless opening g_N^* , opening Γ_f^{open} , and close Γ_f^{stick} areas for the same loading steps and aquifer settings.

By inspection of Figure 7, we can highlight the following results:

1. The regression surface is discontinuous approximately along the straight line $\eta_r = 0.25$ in the plane $(\eta_r, \Delta p)$, where the transition between condition (1) (the rupture does not propagate to the ground surface) and condition (2) (the rupture develops from the ground surface and propagates to join the deep fracture) occurs;
2. The condition (2) occurs for $\eta_r < 0.25$, that is, when the aquifer depth is smaller than 5 to 6 times the aquifer thickness, and $d_{r,act}$ evolves as a quadratic function of η_r and a linear function of Δp ;
3. For $\eta_r > 0.25$, the rupture is confined and does not propagate to the ground surface.

3.2. Test Case B

3.2.1. Model Outcome

Test case B investigates the effects of the variation in thickness of the compacting aquifer system by conceptualizing the schematic configuration of Figure 2b as shown in Figure 8. The active portion of the aquifer has an abrupt increase in thickness from h to h_1 . The analysis is carried out by keeping $h = 60$ m, and varying h_1

Table 2
Statistical Measures of the Model Fit for the Three Test Cases Addressed by the Study

Test case	RMSE		R^2	
	Condition (1)	Condition (2)	Condition (1)	Condition (2)
A	0.09	0.14	0.73	0.96
B	0.05	0.15	0.62	0.99
C	0.00	0.16	1.00	0.93

Table 3
Coefficients of the Models $d_{r,act} = a+bx+cy+dxy+ex^2$ Obtained by Fitting the Numerical Results With a Multivariate Analysis

Test case	Condition	Coefficients				
		<i>a</i>	<i>b</i>	<i>c</i>	<i>d</i>	<i>e</i>
A	1	0.180	-0.401	0.019	-	-
	2	4.785	-41.39	1.116	-4.085	112.52
B	1	-0.951	0.247	0.067	-	-
	2	-1.923	0.506	0.145	-	-
C	1	0.0	0.0	0.0	-	-
	2	-0.344	0.115	0.026	-	-

Note. The variable *x* corresponds to η_r (test case A), h_r (test case B), H_r (test case C), and *y* to Δp (in bar).

from h to $6h$. The average depth of the aquifer is fixed at 250 m. As expected, the continuum stress-strain analysis shows that stress peaks are concentrated around the discontinuity (Figure 9). Hence, the potential rupture surface Γ_f is a vertical plane introduced where the change in aquifer thickness occurs. This configuration conceptualizes the geological setting where ground ruptures occur in Queretaro, Mexico (Carreón-Freyre et al., 2016).

The generation of a ground rupture is investigated as a function of the ratio:

$$h_r = \frac{h_1}{h} \tag{11}$$

varying h_r in the range between 1 and 6. With this configuration, motion along Γ_f can occur. Moreover, the amount of sliding induced by the aquifer depletion (reduction in pore pressure) is smaller than that obtained in test case A. This is expected, because test case A can be interpreted as the limit of test case B for the ratio h_1/h approaching infinity.

As in test case A, two basic mechanisms, denoted as condition (1) and condition (2), can be recognized in test case B depending on h_r . When $h_r \rightarrow 1$, the rupture, if present, remains confined at the aquifer depth. This is shown in Figure 10a for $h_r = 2$ and gives rise to the configuration denoted as condition (1). By distinction, with larger h_r values, the rupture can develop from the ground surface and propagate downward, joining the rupture localized around the interfaces of the active and inactive portions of the aquifer system (Figure 10b). Similarly to test case A, this occurrence is denoted as condition (2). Figures 10c and 10d show that opening extends in depth significantly less than sliding.

3.2.2. Multivariate Analysis

A multivariate analysis was done to define a model describing the behavior of the relative activation depth $d_{r,act}$ (equation (9) where d_1 corresponds to the top depth of the thicker aquifer) as a function of $(h_r, \Delta p)$. The value of $d_{r,act}$ was sampled by varying h_r from 1 to 6, with a unit increment, and considering 10 loading steps with a uniform Δp , for a total number of $n = 60$ evaluations of the state variable. The resulting regression is shown in Figure 11. In this test case, the data set is well represented by a pair of planar surfaces, with a discontinuous behavior along the straight line:

$$h_r = -0.023\Delta p + 3.56 \tag{12}$$

in the $(h_r, \Delta p)$ plane. Generally, Δp has a minor impact on the inception of rupture, which occurs at $h_r \cong 3.5$. The values of *RMSE* and R^2 provided in Table 2 show a satisfactory match between the regression model and the observations. Table 3 provides the coefficients of the approximating planes shown in Figure 11.

Inspection of Figure 11 suggests the following:

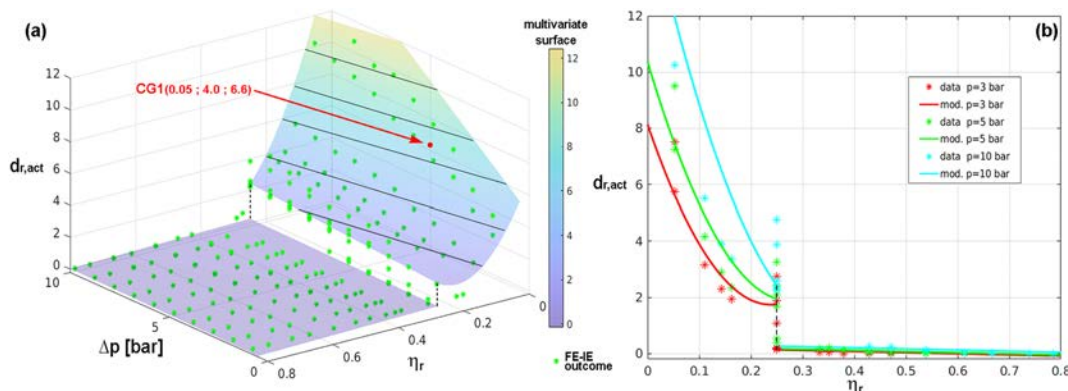


Figure 7. Test case A: (a) 3-D regression surface $d_{r,act} = d_{r,act}(\eta_r, \Delta p)$ obtained by the multivariate analysis. The condition corresponding to rupture 1 in Casa Grande (CG1), see section 4, is provided. (b) Behavior of the 3-D surface for a few Δp values.

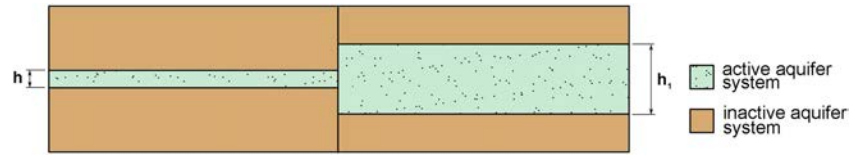


Figure 8. Test case B: Conceptual model of the geological setting. The active and inactive aquifers identify the compacting layer, that is, the geologic unit where pore pressure changes because of groundwater pumping and inactive aquifer where the pore pressure change does not propagate, respectively.

1. As in test case A, the discontinuity along $h_r \cong 3.5$ is due to the transition between condition (1) and condition (2);
2. For $h_r < 3.5$ the rupture does not develop irrespective of the pore pressure decline Δp ;
3. By distinction, for $h_r > 3.5$ the relative activated area $d_{r,act}$ generally tends to increase with a linear trend with both h_r and Δp ;
4. Relative activation depths $d_{r,act}$ are smaller than those computed for test case A.

3.3. Test Case C

3.3.1. Model Outcome

In test case C, the geological setting is characterized by the presence of a bedrock ridge covered by alluvial deposits. We denote by H_t the total thickness of the simulated domain, h the thickness of the active portion of the aquifer, and H_b the height of bedrock ridge, as depicted in Figure 12. This configuration conceptualizes the geological setting where ground ruptures occur in Wuxi, Yangtze deltaic plain, China (Ye et al., 2018).

Aquifer-system compaction is responsible for the land subsidence, which is uniformly distributed except in the central portion of the domain (Figure 13a). The continuum stress/strain analysis clearly reveals the mechanism that can give rise to ruptures. The stiff ridge surrounded by compressing deposits causes horizontal tractions in the alluvial deposits just above the ridge (Figure 13b). At the ground surface, the tensile stress can be approximately 20% of the pore pressure depletion in the active aquifer system. Figure 13c shows that sediment dilatation (red areas) develops in a zone around the apex of the bedrock ridge, and extends to land surface. Conversely, sediment contraction (blue areas) occurs along the base of the ridge near the bottom of the active aquifer system and near land surface at the sides of the large central stretching zone. Generally, because the tensile strength of soils is negligible, the potential for a ground rupture to form above the ridge is high. Consequently, the inner discontinuity surface Γ_f is introduced as a plane along the central

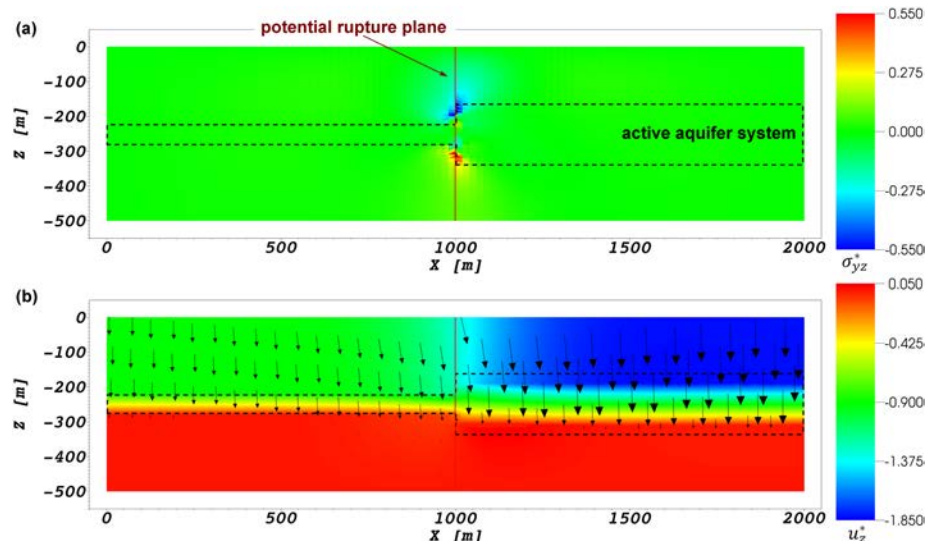


Figure 9. Test case B: (a) shear stress σ_{yz}^* and (b) vertical displacement u_z^* provided by the continuum stress-strain analysis with $h=60$ m and $h_1 = 180$ m. A vector map showing the displacement field is provided in (b).

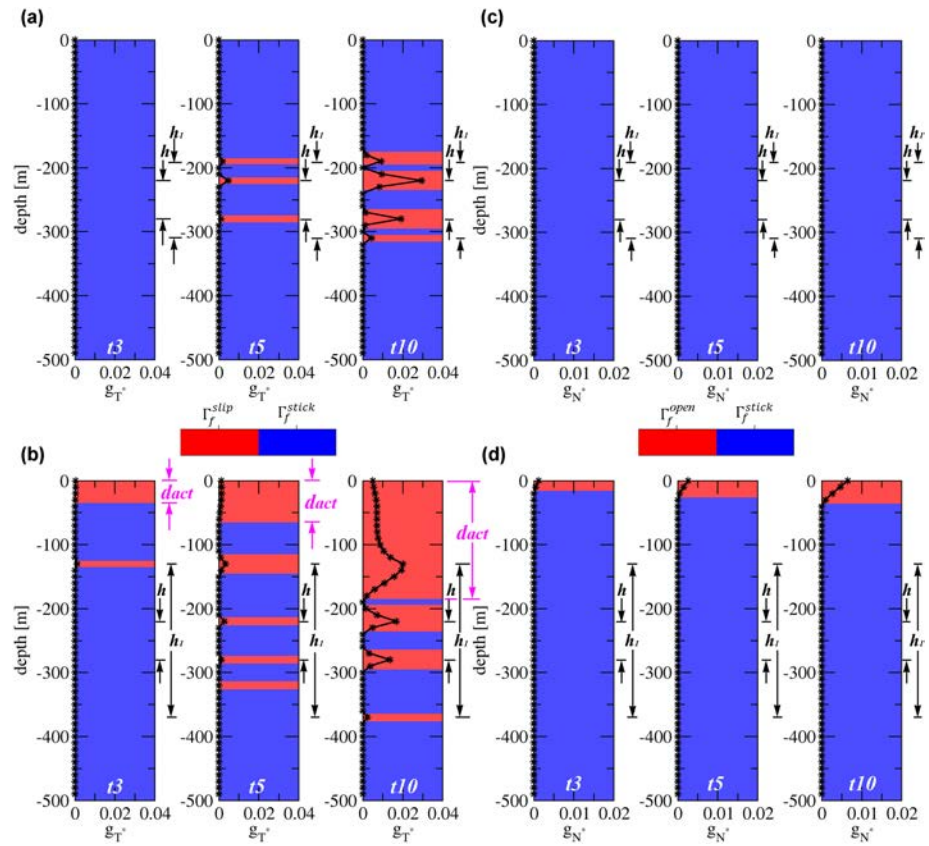


Figure 10. Test case B: (a and b) dimensionless slip g_T^* (dotted black line), sliding Γ_f^{slip} , and close Γ_f^{stick} areas (red and blue zones) for the 3rd, 5th, and 10th loading steps (denoted as t_3 , t_5 , and t_{10} in the figure) obtained for (a) $h_r = 2$ and (b) $h_r = 4$. (c and d) Similar plots are shown for the dimensionless opening g_N^* , opening Γ_f^{open} , and close Γ_f^{stick} areas for the same loading steps and aquifer settings.

vertical section, from the ridge tip to the land surface. Notice that, because of the problem symmetry, the discontinuity or rupture in this case is subject to opening but not sliding motion.

The parametric analysis was done by varying the aquifer thickness h , the ridge height H_b , and the pore pressure decline Δp . In particular, the analysis proceeded in two stages. In the first stage, h was specified at 350 m and H_b was varied. Values of the ratio H_b/H_t were varied in the interval $[0.25; 0.75]$, with $H_t = 500$ m. The results are provided in Figures 14a and 14b. For $H_b/H_t < 0.50$, the rupture remains confined at depth, in correspondence to the aquifer top (condition (1)). For H_b/H_t greater than or equal to about 0.50, the rupture

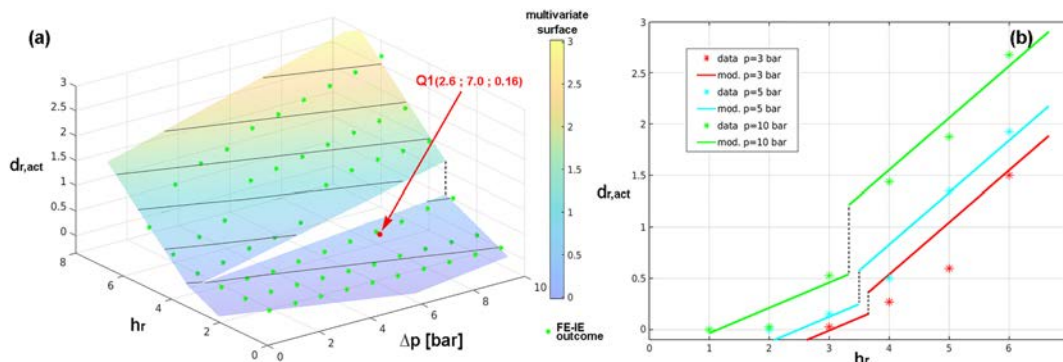


Figure 11. Test case B: (a) 3-D regression surface $d_{r,act} = d_{r,act}(h_r, \Delta p)$ obtained by the multivariate analysis. The condition corresponding to ruptures in Queretaro (Q1), see section 4, is provided. (b) Behavior of the 3-D surface for a few Δp values.

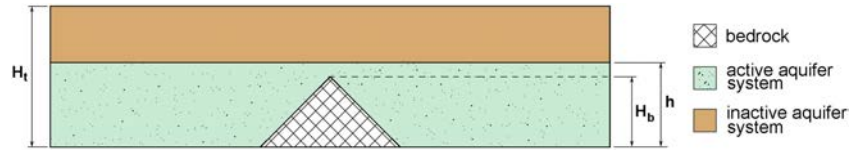


Figure 12. Test case C: Conceptual model of the geological setting. The active and inactive aquifers identify the compacting layer, that is, the geologic unit where pore pressure changes because of groundwater pumping and inactive aquifer where the pore pressure change does not propagate.

develops from the ground surface as well. For $H_b/H_t = 0.75$, the rupture depth is about 30–40 m and the maximum dimensionless opening is approximately 10 times larger than in the case for $H_b/H_t = 0.25$. Although Γ_f^{slip} and Γ_f^{open} coincide, null g_T^* characterizes the rupture due to symmetry (Figures 14a and 14b). In the second stage, H_b/H_t is fixed at 0.75 and h varies between 0 and 400 m. The rupture never propagates at depth to reach the bedrock ridge.

3.3.2. Multivariate analysis

A multivariate analysis was performed to relate the relative activation depth $d_{r,act}$ and the pair of independent variables $(H_r, \Delta p)$. H_r is the ratio between thickness of the aquifer and the depth of the rock ridge tip:

$$H_r = \frac{h}{H_t - H_b} \quad (13)$$

For consistency with equation (13), the definition of $d_{r,act}$ was modified slightly with respect to equation (9) as follows:

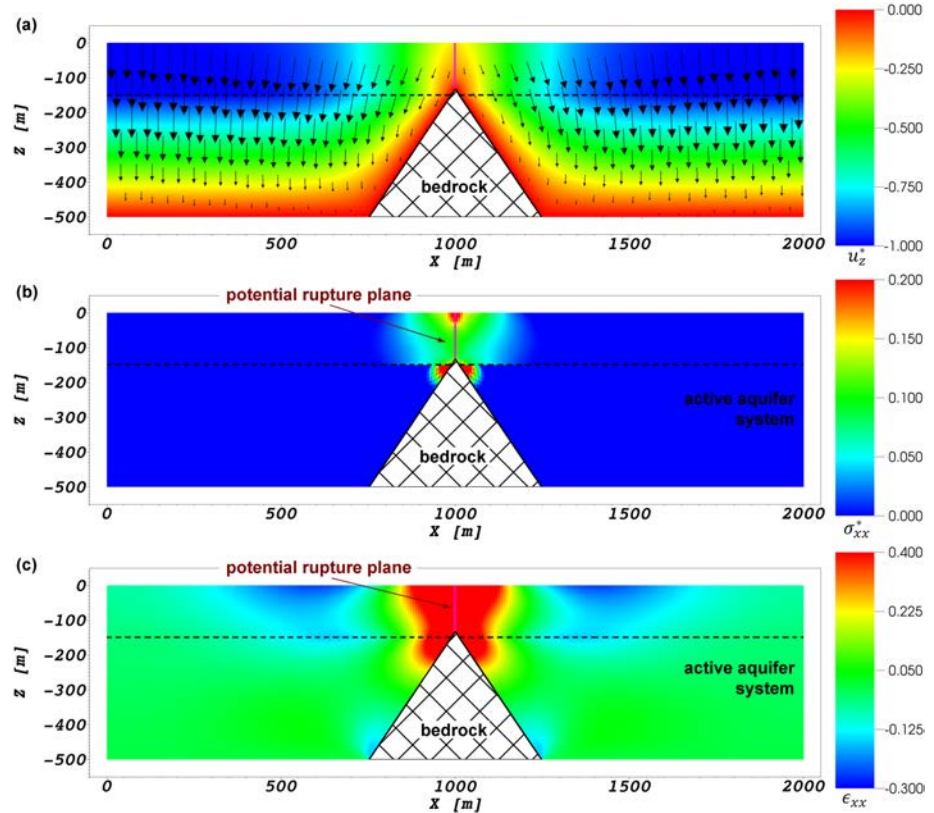


Figure 13. Test case C: (a) vertical displacement u_z^* , (b) normal stress σ_{xx}^* , and (c) horizontal strain ϵ_{xx} provided by the continuum stress-strain analysis with $h = 375$ m, that is, $h/H_t = 0.75$, and $H = 350$ m. A vector map showing the displacement field is provided in (a).

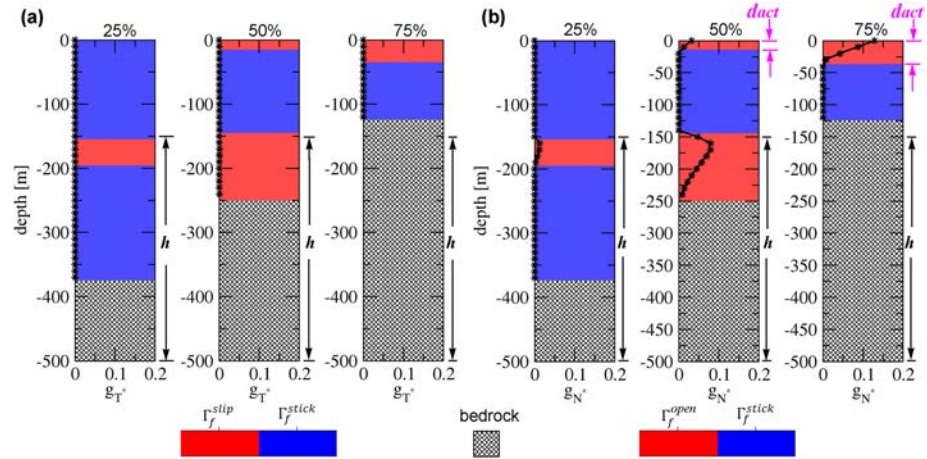


Figure 14. Test case C: (a) dimensionless slip g_T^* (dotted black line), sliding Γ_f^{slip} , and close Γ_f^{stick} areas (red and blue zones) for $H_b/H_t = 0.25, 0.50,$ and 0.75 . Similar plots are shown in (b) for the dimensionless opening g_N^* , opening Γ_f^{open} , and close Γ_f^{stick} areas for the same aquifer settings.

$$d_{r,act} = \frac{d_{act}}{H_t - H_b} \quad (14)$$

The regression surface is given in Figure 15. In this case, the model outcomes are well matched by a pair of planes with a discontinuous behavior along the straight line defined by

$$H_r = -0.176\Delta p + 2.61 \quad (15)$$

in the plane $(H_r, \Delta p)$. The satisfactory fit of the regression model is confirmed by the $RMSE$ and R^2 values provided in Table 2. The coefficients of the 3-D approximating surfaces are given in Table 3.

Inspection of Figure 15 suggests the following:

1. Opening prevails over sliding; however, this is due to the symmetry of the geometric configuration. In nature, both opening and sliding are expected to occur;
2. Depth of the bedrock ridge and, secondarily, the thickness of the active portion of the aquifer system are the key parameters for rupture inception. Rupture at the ground surface is more prone to occur as the ridge tip becomes shallower, corresponding to $H_b/H_t > 0.50$ for the present configuration. Rupture propagation at depth tends to increase linearly with the thickness of the compacting deposits;
3. Pore pressure change plays a more important role than in the other test cases, because it controls the differential subsidence between the area above the ridge tip and the sides. The inception of ground rupture occurs for lower values of $h/(H_t - H_b)$, that is, thinner active aquifer system or deeper ridge tip, as Δp increases.

4. Discussion

Ground ruptures accompanying aquifer-system compaction and land subsidence is an induced process that is occurring more frequently worldwide. Initially recognized in the early 1950s in Arizona (Feth, 1951), ground ruptures have been reported since the 1970s in other states in the southwest United States (e.g., Holzer et al., 1979; Jachens & Holzer, 1979), since the early 1990s in Queretaro, Mexico (e.g., Trejo-Moedano & Martinez-Baini, 1991), and China (e.g., Lee et al., 1996), and since the start of the new millennium in Saudi Arabia, Iran, and other arid and semiarid zones in various countries of Asia and Africa. The relevant scientific publications mainly focus on the distribution of the ruptures at the land surface, and unfortunately, little information about the geological setting and evolution of groundwater-level declines and groundwater depletion is available in most of the cases.

To test the reliability of hypothetical modeling outcomes developed in this study, we compare the results described above with three well-documented cases of subsiding areas where subsidence was attributed to aquifer-system compaction and where ground ruptures were reported. These cases pertain to Casa Grande in the Picacho Basin, Arizona, USA, Queretaro, Mexico, and Wuxi, China (Figure 16).

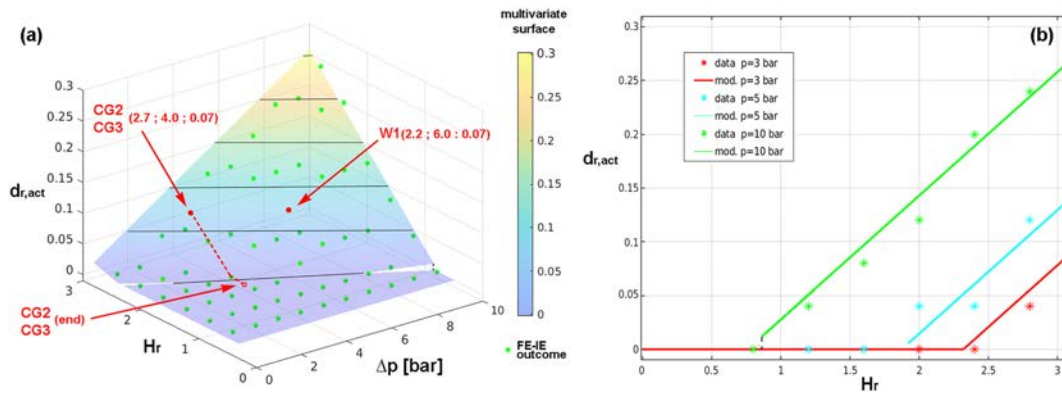


Figure 15. Test case C: (a) 3-D regression surface $d_{r,act} = d_{r,act}(H_r, \Delta p)$ obtained by the multivariate analysis. The conditions corresponding to ruptures 2 and 3 in Casa Grande (CG2, CG3) and the rupture in Wuxi (W1), see section 4, are provided. In Casa Grande, ruptures 2 and 3 propagate until the condition represented by the red-empty dot is realized. (b) Behavior of the 3-D surface for a few Δp values.

In Casa Grande, Arizona Jachens and Holzer (1982) carried out precise gravity and magnetic surveys across ground failure zones showing that ruptures in the alluvial deposits developed in correspondence with local high elevation of the buried bedrock surface where the buried bedrock surface exhibited relatively large convex-upward changes in slope. Figure 16a (top) shows a map of superimposed rupture traces in the early 1970s and bedrock depth, and the elevation profile of the top of the buried bedrock along a section crossing three main ruptures (bottom). Test case A (i.e., outcropping bedrock laterally bounding the aquifer system) can be associated with the hydrogeologic conditions of rupture 1 and test case C (i.e., a buried bedrock ridge intruding on the aquifer system) can be associated with the hydrogeologic conditions of ruptures 2 and 3. Because of the lack of more specific hydrogeologic information, we can grossly assume that the top and bottom of the active aquifer system are represented by the water table and the bedrock, respectively. Therefore, rupture 1, with $d_1/d_2 \cong 10/200 \cong 0.05$, that is, $\eta_r < 0.25$, satisfies the condition (2) (i.e., rupture development and propagation) requirements (see Figure 7). In relation to ruptures 2 and 3, the estimated values of the key parameters are $h \cong 240$ m, $H_r \cong 260$ m, $H_b \cong 170$ m, and $H_r \cong 2.7$. If $\Delta p \cong 4$ bar, the site can be characterized by a condition (2) behavior favorable to ruptures (Figure 15). Interestingly, the map in Figure 16a shows that the extents of the surface traces of ruptures 2 and 3 correspond to bedrock depths less than about 140–150 m, that is, $H_b \cong 120$ m and $H_r \cong 1.7$. Consistent with this observation, the parameter pair $(H_r, \Delta p) = (1.7, 4.0)$ is near the threshold between condition (1) (i.e., no rupture) and condition (2) in Figure 15. Though, no record of the rupture depth d_{act} is available, it can be estimated from the multivariate analysis. The use of Table 3 (test case C, condition 2) with the parameter pair (2.7, 4.0) provides $d_{r,act} = 0.07$, that is, d_{act} on the order of 5–6 m (equation (14)). Photos of the area taken in the 1960s show ruptures characterized by a depth with metric order of magnitude (Robinson & Peterson, 1962).

Queretaro is a city located in the central Trans-Mexican Volcanic Belt on a continental basin filled with lacustrine and alluvial sediments, pyroclastic deposits, and interbedded fractured basalts (Ochoa-González et al., 2018). Due to the presence of north-south trending normal faults, the depths and thicknesses of the filling compressible materials vary many tens of meters in short distances (Figure 16b, bottom). Groundwater pumping caused a piezometric lowering of about 70 m over the last 50 years, with significant land subsidence (as much as 2.5 m) and the development of ground ruptures in locations corresponding to the locations of buried faults (Figure 16b; Carreón-Freyre et al., 2016). The hydrogeologic setting is analogous to that of test case B (i.e., an abrupt change of aquifer geometry). The compressible deposits are represented by the Tp Ar-Cg and Tom Py-Lac stratigraphic units (Figure 16b). In correspondence with the change in aquifer geometry imposed by the Central Fault system (Figure 16b, bottom), their cumulative thicknesses are $h \cong 80$ m and $h_1 \cong 10$ m, with $h_r \cong 2.6$. Using $\Delta p \cong 7$ bar, the parameter pair $(h_r, \Delta p)$ characterizes a condition (1) state (i.e., a limited propagation of the rupture; Figure 11), with $d_{r,act} = 0.16$ (Table 3). Therefore, equation (9) provides $d_{act} \cong 1.5$ m using a specified 10-m depth for the top of Tp Ar-Cg. Measurements of rupture depth and rupture sliding are unavailable, but an estimate of 1–2 m of rupture sliding can be derived from the photos published in the literature (e.g., Carreón-Freyre et al., 2016; Ochoa-González et al., 2018).

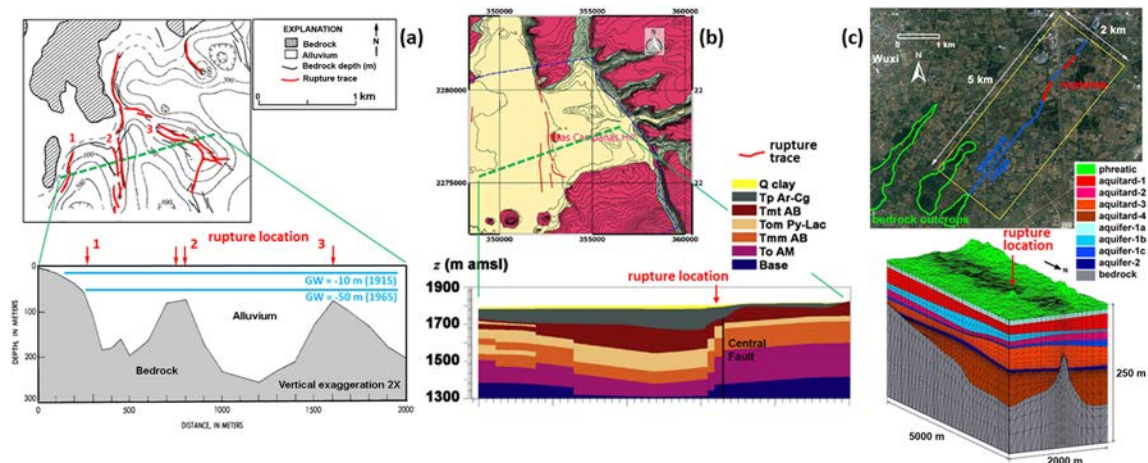


Figure 16. Case studies of ground ruptures caused by groundwater pumping: (a) Casa Grande, Arizona, USA (modified after Jachens and Holzer (1982)); (b) Querétaro, Mexico (modified after Ochoa-González et al. (2018)); and (c) Wuxi, China (modified after Ye et al. (2018)). A map with the main topographic features and the rupture trace (above) and a representation of the main geological features (below) are provided for each site. The rupture locations are shown by red alignments in the maps and red arrows in the geologic conceptual models. Definitions of stratigraphic symbols shown in (b): Q Clay: Quaternary lacustrine, surficial clays and low-permeable relatively thin deposits; Tp Ar-Cg: Sediments and volcanic rocks representing the main porous unit; Tmt AB: Volcanic sequence comprising andesites, basalts and lava flows representing a highly fractured unit; Tom Py-Lac: pyroclastic and lacustrine deposits forming the second main porous unit; Tmm AB: older andesitic and basaltic fractured unit; To AB: Andesitic and basaltic less fractured unit; Base: Hydrogeological basement comprising low permeability, rigid rocks.

The last case study is Wuxi, Jiangsu Province, China. Excessive exploitation of groundwater in Wuxi started in the 1970s, and resulted in as much as 2.5 m of land subsidence between 1970 and 2013. The first ground rupture in the Wuxi area was reported in 1989 and more than 20 ruptures had developed by 2000 when the local government stopped groundwater pumping (Ye et al., 2016). The maximum piezometric decline of 60 m occurred in the second confined aquifer (aquifer-2, Figure 16c) between 1999 and 2005. The fissures are grouped with a banded distribution, whose orientation is aligned with the bedrock ridges buried by the Yangtze alluvial deposits and partially outcropping in the sedimentary plain (Figure 16c). Specific monitoring surveys and a modeling study have been recently carried out for one of the ruptures (Ye et al., 2018). The hydrogeologic setting in Wuxi conforms to the setting posed in test case C, although the multilayered aquifer system is more complex than that represented in Figure 12, with four confined aquifers and four intervening aquitards. The following values can be used to compare the Wuxi case study with the outcome of the multivariate model shown in Figure 15: $h \cong 130$ m, $H_b \cong 110$ m, and $H_t \cong 170$ m, resulting in $H_r \cong 2.2$, with $\Delta p \cong 6$ bar. The parameter pair $(h_r, \Delta p)$ corresponds to condition (2) (Figure 15), that is, rupture development, consistent with the occurrence in Wuxi. Using the parameters provided in Table 3, $d_{r,act} \cong 0.07$ and, consequently, $d_{act} \cong 4.5$ m. This value is smaller than the 10–15-m estimate of the rupture depth (determined in situ by inserting a steel-rod into the rupture) and the 20–30-m value estimated from numerical modeling results (Ye et al., 2018). However, accounting for the simplifications introduced in this analysis, the differences are reasonable.

A number of simplifications have been introduced in the present investigation. The hydrogeologic settings are idealized and quite simple, the effects of changes in the saturated thickness of shallow (phreatic) aquifers are not addressed, and possible spatial gradients in the pore pressure changes are not considered. From the mechanical point of view, simple linear rock properties are used and weakening of rupture surfaces is not accounted for. These simplifications can be mitigated when a modeling analysis is developed for a specific case study. The geomechanical simulator used in this study, GEPS3D (Geomechanical Elasto-Plastic Simulator; e.g., Janna et al., 2012; Franceschini et al., 2016; Ye et al., 2018), can simulate complex hydrogeologic systems with nonlinear elasto-visco-plastic sediment rheology and failure parameters that change once the rupture has been initiated. Nevertheless, the above comparisons suggest that the principal features governing rupture generation in basins undergoing aquifer-system compaction and the accompanying land subsidence have been adequately addressed.

Possible mechanisms of rupture generation have been qualitatively delineated since the 1990s (Sheng et al., 2003; Sheng & Helm, 1998), and theoretically analyzed via simple analytical models (Budhu & Shelke, 2008). In this contribution we quantitatively investigate for the first time how the aquifer-system geometry and groundwater-level decline influence rupture development. As observed in previous works, hydrogeologic discontinuities play a key role. However, abrupt changes in soil compressibility and, secondarily, hydraulic conductivity are not sufficient to cause rupture development. The principal driving mechanisms are related to changes in the stress and strain fields caused by pore pressure depletion. The larger and closer to land surface the hydrogeologic discontinuity is, the smaller the pressure change required to initiate ground rupturing is. A set of parametric equations has been provided to distinguish whether a particular hydrogeologic setting is prone to ground ruptures and to quantify maximum depths of rupture propagation.

5. Summary and Conclusions

The research presented here used numerical modeling to simulate three idealized, conceptual hydrogeologic settings that are likely to produce the inception and growth of ground ruptures due to groundwater withdrawal. The original numerical formulation developed by Franceschini et al. (2016, 2019) was used to carry out a parametric study addressing each of three main mechanisms of aseismic rupture inception and propagation implemented in test cases A, B, and C, respectively: (i) test case A—an aquifer system comprising sedimentary and volcanoclastic materials filling a graben, (ii) test case B—differential compaction due to the variation in thickness of the aquifer system, and (iii) test case C—presence of a bedrock ridge underlying and intruding upon an aquifer system.

The simulation results were processed with the aid of a multivariate regression analysis, in order to evaluate the relationships between rupture occurrence, the dimensionless geometric parameters characterizing the conceptual hydrogeologic models and the pore pressure change in the aquifer system. Based on the modeling analysis, the following summarizes the results and conclusions derived for the three test cases:

1. Test case A: A ground rupture is more likely to develop for thick and/or shallow aquifer systems. For the conceptual hydrogeologic configuration analyzed in this test case, the inception of a ground rupture is practically independent of Δp and occurs when the depth of the aquifer top is less than 0.25 times the depth of the aquifer bottom. Once initiated, the extent of rupture propagation is governed by the pore pressure change Δp and increases with Δp ;
2. Test case B: A ground rupture tends to develop for abrupt changes in aquifer thickness. In the prescribed conceptual hydrogeologic configuration, the rupture can be initiated even for small Δp where the ratio between the thicknesses of adjacent aquifers h_r is about 3.5. Once initiated, the extent of the rupture propagation varies almost linearly with both h_r and Δp ;
3. Test case C: A tensile stress regime develops around the bedrock ridge owing to differential compaction of the aquifer system. The rupture propagates downward from the land surface when the bedrock ridge is sufficiently close to the land surface and the pressure decline in the aquifer is sufficiently large. In the conceptual scheme analyzed herein, both geometric parameters and pressure variation play a similar role. A ground rupture is likely to develop if the ratio between the depth of the active aquifer top and the bedrock ridge H_r is approximately greater than $2.6 - 0.18\Delta p$, with Δp in units of bar. After inception, the rupture extent evolves linearly with both H_r and Δp .

The role of Δp in driving the generation of ground ruptures increases progressively from the mechanism analyzed in test case A to the mechanism of test case C. The value of Δp also plays a major role in the magnitude of opening and/or sliding of the rupture.

Comparisons between the observations available for three documented field cases (USA, Mexico, China) and the modeling outcomes presented here support the validity of the analysis developed in this work.

References

- Abidin, H. Z., Andreas, H., Gumilar, I., Fukuda, Y., Pohan, Y. E., & Deguchi, T. (2011). Land subsidence of Jakarta (Indonesia) and its relation with urban development. *Natural Hazards*, 59(3), 1753–1771.
- Budhu, M., & A. Shelke (2008). The formation of earth fissures due to groundwater decline. In D. N. Singh (Ed.), Proc. 12th International Conference of the International Association of Computer Methods and Advances in Geomechanics (pp. 3051–3059).

Acknowledgments

This work is a contribution to International Geoscience Programme (IGCP) Project 641: “Mechanisms, Monitoring, and Modeling Earth Fissure Generation and Fault Activation due to Subsurface Fluid Exploitation (M3EF3)” (<https://www.igcp641.org/>). The research has been partially funded by Open Project 20170301 of the Key Laboratory of Earth Fissures Geological Disaster, Ministry of Land and Resources, Geological Survey of Jiangsu Province (China), and by Project 41877180 of the National Natural Science Foundation of China. Reviews by Jean Bahr (Editor, WRR journal), William Haneberg (State Geologist and Director, Kentucky Geological Survey; Research Professor of Earth & Environmental Sciences, University of Kentucky), two anonymous reviewers and Michelle Sneed (U. S. Geological Survey) greatly improved the manuscript. The data used in this study can be http://www.igcp641.org/?page_id=918 (data set used in the publication “A parametric numerical analysis of factors controlling ground ruptures caused by groundwater pumping” by Matteo Frigo, Massimiliano Ferronato, Jun Yu, Shujun Ye, Devin Galloway, Dora Carreón-Freyre, and Pietro Teatini, *Water Resources Research*, 2019).

- Carreón-Freyre, D. (2010). Land subsidence processes and associated ground fracturing in Central Mexico. In D. C. Freyre, M. Cerca, & D. L. Galloway (Eds.), *Land Subsidence, Associated Hazards and the Role of Natural Resources Development* (Vol. 339, pp. 149–157). Wallingford UK: IAHS Publ.
- Carreón-Freyre, D., Cerca, M., Ochoa-González, G., Teatini, P., & Zuniga, F. R. (2016). Shearing along faults and stratigraphic joints controlled by land subsidence and hydraulic gradient in the Valley of Queretaro, Mexico. *Hydrogeology Journal*, 24(3), 657–674.
- Choubin, B., Mosavi, A., Alamdarloo, E. H., Hosseini, F. S., Shamsheband, S., Dashtekian, K., & Ghamisi, P. (2019). Earth fissure hazard prediction using machine learning models. *Environmental Research*, 179(Pt A). <https://doi.org/10.1016/j.envres.2019.108770>
- Conway, B. D. (2016). Land subsidence and earth fissures in south-central and southern Arizona, USA. *Hydrogeology Journal*, 24(3), 649–655.
- Feth, J. H. (1951). Structural reconnaissance of the Red Rock Quadrangle, Arizona. U. S. Geological Survey, Open-File Report 51–199, 32 pp.
- Franceschini, A., Castelletto, N., & Ferronato, M. (2019). Block preconditioning of fault/fracture mechanics saddle-point problems. *Computer Methods in Applied Mechanics and Engineering*, 344, 376–401.
- Franceschini, A., Ferronato, M., Janna, C., & Teatini, P. (2016). A novel Lagrangian approach for a stable numerical simulation of the mechanics of faults. *Journal of Computational Physics*, 314, 503–521.
- Galloway, D. L., & Riley, F. S. (1999). San Joaquin Valley, California - Largest human alteration of the Earth's surface. In D. L. Galloway, D. R. Jones, & S. E. Ingebritsen (Eds.), *Land Subsidence in the United States* (Vol. 1182, pp. 23–34). U.S. Geological Survey Circular. <http://pubs.usgs.gov/circ/circ1182/>
- Gambolati, G., & Teatini, P. (2015). Geomechanics of subsurface water withdrawal and injection. *Water Resources Research*, 51, 3922–3955. <https://doi.org/10.1002/2014WR016841>
- Gambolati, G., Teatini, P., Baù, D., & Ferronato, M. (2000). Importance of poroelastic coupling in dynamically active aquifers of the Po river basin, Italy. *Water Resources Research*, 36, 2443–2459.
- González, P. J., Tiampo, K. F., Palano, M., Cannavò, F., & Fernández, J. (2012). The 2011 Lorca earthquake slip distribution controlled by groundwater crustal unloading. *Nature Geoscience*, 5, 821–825.
- Hager, C., Hueber, S., & Wolmuth, B. I. (2008). A stable energy-conserving approach for frictional contact problems based on quadrature formulas. *International Journal for Numerical Methods in Engineering*, 73(2), 205–225.
- Hernandez-Marin, M., & Burbey, T. J. (2010). Controls on initiation and propagation of pumping-induced earth fissures: Insights from numerical simulations. *Hydrogeology Journal*, 18(8), 1773–1785.
- Hernandez-Marin, M., & Burbey, T. J. (2012). Fault-controlled deformation and stress from pumping-induced groundwater flow. *Journal of Hydrology*, 428–429, 80–93.
- Hoffman, J., Leake, S. A., Galloway, D. L., & Wilson, A. M. (2003). MODFLOW-2000 ground-water model — User guide to the subsidence and aquifer-system compaction (SUB) package. U.S. Geological Survey Open-File Report 2003-233, 44 p. <http://pubs.usgs.gov/of/2003/of03-233/>, accessed September 22, 2019.
- Holzer, T. L., Davis, S. N., & Lofgren, B. E. (1979). Faulting caused by groundwater extraction in southcentral Arizona. *Journal of Geophysical Research*, 84(B2), 603–612.
- Isotton, G., Teatini, P., Ferronato, M., Janna, C., Spiezia, N., Mantica, S., & Volontè, G. (2019). Robust numerical implementation of a 3D rate-dependent model for reservoir geomechanical simulation. *International Journal for Numerical and Analytical Methods in Geomechanics*, 1–20. <https://doi.org/10.1002/nag.3000>
- Jachens, R. C., & Holzer, T. L. (1979). Geophysical investigations of ground failure related to groundwater withdrawal - Picacho Basin, Arizona. *Ground Water*, 17(6), 574–585.
- Jachens, R. C., & Holzer, T. L. (1982). Differential compaction mechanism for earth fissures near Casa Grande, Arizona. *Geological Society of America Bulletin*, 93, 998–1012.
- Jaeger, J. C., & Cook, N. G. W. (1979). *Fundamentals of Rock Mechanics*. London: Chapman & Hall.
- Janna, C., Castelletto, N., Ferronato, M., Gambolati, G., & Teatini, P. (2012). A geomechanical transversely isotropic model of the Po River basin using PSInSAR derived horizontal displacement. *International Journal of Rock Mechanics and Mining Sciences*, 51, 105–118.
- Kikuchi, N., & J. T. Oden (1988). Contact Problems in Elasticity: A Study of Variational Inequalities and Finite Element Methods. Society for Industrial and Applied Mathematics, Philadelphia.
- Klose, C. D. (2007). Mine water discharge and flooding: A cause of severe earthquakes. *Mine Water and the Environment*, 26, 172–180.
- Kundu, B., Vissa, N. K., & Gahalaut, V. K. (2015). Influence of anthropogenic groundwater unloading in Indo-Gangetic plains on the 25 April 2015 Mw 7.8 Gorkha, Nepal earthquake. *Geophysical Research Letters*, 42, 607–10,613. <https://doi.org/10.1002/2015GL066616>
- Leake, S. A., & Galloway, D. L. (2007). MODFLOW ground-water model — User guide to the Subsidence and Aquifer-System Compaction Package (SUB-WT) for Water-Table Aquifers. U.S. Geological Survey Techniques and Methods Report 6–A23, 42 p. <http://pubs.usgs.gov/tm/2007/06A23/>, accessed September 22, 2019.
- Lee, C. F., Zhang, J. M., & Zhang, Y. X. (1996). Evolution and origin of the ground fissures in Xian, China. *Engineering Geology*, 43, 45–55.
- Li, Y., Yang, J., & Hu, X. (2000). Origin of ground fissures in the Shanxi Graben System, Northern China. *Engineering Geology*, 55, 267–275.
- Ochoa-González, G. H., Carreón-Freyre, D., Franceschini, A., Cerca, M., & Teatini, P. (2018). Overexploitation of groundwater resources in the faulted basin of Querétaro, Mexico: a 3D deformation and stress analysis. *Engineering Geology*, 245, 192–206.
- Pacheco, J., Arzate, J., Rojas, E., Arroyo, M., Yutis, V., & Ochoa-González, G. H. (2006). Delimitation of ground failure zones due to land subsidence using gravity data and finite element modeling in the Quertaro valley. *Mexico, Engineering Geology*, 86, 143–160.
- Panda, B. B., Rucker, M. L., & Ferguson, K. C. (2015). Modeling of earth fissures caused by land subsidence due to groundwater withdrawal. *Proc IAHS*, 372, 69–72.
- Peng, J. B., Sun, X. H., Wang, W., & Sun, G. C. (2016). Characteristics of land subsidence, earth fissures and related disaster chain effects with respect to urban hazards in Xian, China. *Environmental Earth Sciences*, 75(16), 1–15. <https://doi.org/10.1007/s12665-016-5928-3>
- Plaxis (2017). Plaxis 3D Reference Manual, 470 pp. <https://www.plaxis.com/product/plaxis-3d/>, accessed September 22, 2019.
- Robinson, G. M., & Peterson, D. E. (1962). Notes on earth fissure in South Arizona. *Geological Survey Circular*, 466, 7. <https://pubs.usgs.gov/circ/1962/0466/report.pdf>
- Rucker, M. L., Ferguson, K. C., & Smilovsky, D. (2019). The Pixley fissure revisited - Understanding an old geohazard to safeguard new infrastructure. In A. Shakoob & K. Cato (Eds.), *LAEG/AEG Annual Meeting Proceedings, San Francisco, California, 2018* (Vol. 5, pp. 69–76). Cham, Switzerland: Springer.
- Sheng, Z., & Helm, D. C. (1998). Multiple steps of earth fissuring caused by ground-water withdrawal. In J. Borchers (Ed.), *Current Research and Case Studies: Proceedings of the Joseph F. Poland Symposium on Land Subsidence* (pp. 229–238). Belmont CA: Star Publ. Co.
- Sheng, Z., Helm, D. C., & Li, J. (2003). Mechanisms of earth fissuring caused by groundwater withdrawal. *Environmental & Engineering Geoscience*, 9(4), 313–324.

- Simo, J. C., & Hughes, T. J. R. (2000). *Computational Inelasticity*. New York: Springer.
- Teatini, P., Carreón-Freyre, D., Ochoa-González, G., Ye, S., Galloway, D., & Hernández-Marin, M. (2018). Ground ruptures attributed to groundwater overexploitation damaging Jocotepec city in Jalisco, Mexico: 2016 field excursion of IGCP-641. *Episodes*, *41*(1), 69–73.
- Teatini, P., Ferronato, M., Gambolati, G., Bertoni, W., & Gonella, M. (2005). A century of land subsidence in Ravenna, Italy. *Environmental Geology*, *47*(6), 831–846.
- Trejo-Moedano, A., & Martínez-Baini, A. (1991). Agrietamiento de suelos zona Querétaro. In *Agrietamientos de Suelos* (pp. 67–74). México.: Sociedad Mexicana de Mecánica de Suelo.
- van Wees, J. D., Buijze, L., Van Thienen-Visser, K., Nepveu, M., Wassing, B. B. T., Orlic, B., & Fokker, P. A. (2014). Geomechanics response and induced seismicity during gas field depletion in the Netherlands. *Geothermics*, *52*, 206–219.
- Wriggers, P. (2005). *Contact Mechanics*. Berlin: Springer.
- Ye, S., Franceschini, A., Zhang, Y., Janna, C., Gong, X., Yu, J., & Teatini, P. (2018). A novel approach to model earth fissure caused by extensive aquifer exploitation and its application to the Wuxi case, China. *Water Resources Research*, *54*, 2249–2269. <https://doi.org/10.1002/2017WR021872>
- Ye, S., Luo, Y., Wu, J., Yan, X., Wang, H., Jiao, X., & Teatini, P. (2016). Three-dimensional modeling of land subsidence in Shanghai, China. *Hydrogeology Journal*, *24*(3), 695–709. <https://doi.org/10.1007/s10040-016-1382-2>
- Ye, S., Xue, Y., Wu, J., Yan, X., & Yu, J. (2016). Progression and mitigation of land subsidence in China. *Hydrogeology Journal*, *24*(3), 685–693.
- Zhang, Y., Wang, Z., Xue, Y., Wu, J., & Yu, J. (2016). Mechanisms for earth fissure formation due to groundwater extraction in the Su-Xi-Chang area, China. *Bulletin of Engineering Geology and the Environment*, *75*, 745–760.
- Ziaie, A., Kumarci, K., Ghanizadeh, A. R., & Mahmodinejad, A. (2009). Prediction of earth fissures development in Sirjan. *Research Journal of Environmental Sciences*, *3*(4), 486–496.
- Zoback, M. D. (2007). *Reservoir Geomechanics*. Cambridge, UK: Cambridge University Press.